Simplified Aerostructural Static Model for Inflated Wings

Yaniv C. Gal-Rom* and Daniella E. Raveh†
Technion—Israel Institute of Technology, Haifa 32000, Israel

DOI: 10.2514/1.J050521

A simplified model for analysis of the aerostructural characteristics of multicell baffled inflated wings is presented. The proposed scheme is an iterative procedure based on a beam theory and strip theory that computes the combined stresses due to inflation pressure and due to aeroelastic loading on a multicell wing, accounting for large wing deflections. Wrinkling criterion on the minimal low principal stress and failure criterion on the maximal high principal stress are applied. Together they define envelopes of allowed combinations of inflation pressure and wing loading, or flight dynamic pressure. These envelopes can be generated per wing geometry and material properties and provide guidelines for the design and analysis of inflated wings. The methodology was validated on a single-cell wing, comparing results with analytical failure criteria from the literature. The methodology was then applied to multicell wings of various geometries, studying the effect of wing aspect ratio, wing thickness ratio, and membrane thickness on the allowed wing loading and allowed and required inflation pressure ranges. The methodology enables a preliminary estimate of an inflated wing's performance and can provide a valuable tool for preliminary design and configuration selection.

Nomenclature

A	=	area, section area, m
AR	=	aspect ratio
C	=	chordwise force, N
C_L	=	lift coefficient
C_{l_α}	=	airfoil lift-curve slope, 1/rad
c	=	wing chord, m
D	=	drag force, N
E	=	elastic (Young's) modulus, N/m^2
F	=	lateral force, N
F_w	=	lateral load at incipient wrinkling, N
G	=	shear modulus, N/m^2
H	=	circumferential tangent (hoopwise) coordinate
I	=	area moment of inertia, m^4
J	=	polar moment of inertia, m^4
L	=	lift force, N
l	=	length, wing semispan, m
M	=	moment, N · m
N	=	normal force, N
P	=	axial load, N/m^2
p	=	inflation pressure, N/m^2
q	=	dynamic pressure, N/m^2
q_d	=	divergence dynamic pressure, N/m^2
q_{xy}	=	shear flow, N/m
$\mathbf{R}$	=	sectional aerodynamic force resultant, N
$\mathbf{r}$	=	radius vector, m
r	=	radius, m
S	=	shear force, N/m^2
s	=	spanwise coordinate
T	=	torsion moment, N · m
T_w	=	torsion moment at incipient wrinkling, N · m
t	=	airfoil thickness, m

t_s	=	membrane thickness, m
V_x, V_z	=	velocity components, m/s
α	=	angle of attack
Δx	=	aerodynamic torsion-moment arm normalized by chord
δ_w	=	deflection/rotation at incipient wrinkling
ν	=	Poisson's ratio
ρ	=	density, kg/m^3
σ	=	tensile stress, N/m^2
τ	=	shear stress, N/m^2
ϕ, θ, ψ	=	angular angles, rad
φ	=	circumferential angle, rad

*Graduate Student, Faculty of Aerospace Engineering. Student Member AIAA.

†Senior Lecturer, Faculty of Aerospace Engineering. Senior Member AIAA.

I. Introduction

INFLATED aircraft structures have been proposed since the 1930s. Simpson et al. [1,2] briefly describe notable designs, indicating an increased interest in the field over the years. New applications, as well as old ones, may benefit from the ability to use inflated members as part of their primary structure. A special interest arises from the potential use of inflation for wing structures, as this may benefit the fields of deployable and morphing aerial vehicles. Design of inflated-structure wings requires particular models and analysis methods to study the properties and limitations of such structures. The current study proposes a simplified analytical model for the structural and aeroelastic characteristics of an inflated wing. Specifically, it evaluates the aeroelastic loads on an inflated wing of large deflections as a function of its geometrical and material properties and inflation pressure. Stresses due to external aeroelastic loading and due to internal inflation-pressure are computed and used to define feasible operation regions in terms of inflation pressure and wing loading or dynamic pressure.

Several papers on the theoretical analysis of inflatable structural members were published during the second half of the 20th century. Most were about cylindrical beams subject to tip load. Stein and Hedgepeth [3] formulated the stress criterion of membrane wrinkling: since a membrane possesses no bending stiffness, it cannot carry compressive stress. When both principal stresses are positive, the membrane is in tension (taut), while if both principal stresses are zero, the membrane is unloaded. Stein and Hedgepeth therefore concluded that when the membrane is wrinkled, it must have one stress that is zero and the other nonzero. From the principal stress expression they derived a wrinkling condition, by requiring vanishing of a principal stress. This condition served as a failure criterion for inflated membranes in studies that followed Stein and Hedgepeth, including the current work. In the case of an inflated

wing, it enables the formulation of a condition on the required and allowable inflation stress range. Comer and Levy [4] used a simplified approach to the wrinkling problem of an inflated beam, subject to lateral tip load. They presented a superposition method of stress due to load and stress due to inflation pressure, yielding the total stress on the structure. Comer and Levy's study is referenced by many papers concerning aerial inflated structures. However, the shortcoming of their study is that it did not include torsion of the beam, an essential part of the loads array over a wing structure. Webber [5] expanded on the work of Comer and Levy [4] to include torsion, enabling better modeling of the wing as an inflated beam made of membrane material. The model presented by Webber serves as the basic model for stress analysis in the current study. Recently, Veldman [6] expanded on Webber's [5] work, proposing treatment of materials that exhibit significant out-of-plane stiffness in low inflation-pressure. Veldman's [6] work also dealt with conical tubes, showing that the section with the smallest radius is most susceptible to wrinkling. Both Webber's [5] and Veldman's [6] analyses were restricted to circular cylindrical beams of a single-cell box section, while a typical inflated-wing structure is composed of a multicell box section, in which shear distribution is considerably more complex. Harvey [7] presented methods for design and analysis of pressure vessels. His work suggested formulas for stress evolution in thin-walled cylindrical pressure vessels and discussed failure criteria. The current study expands on Harvey's work to treat the case of a pressure vessel with several cells of different radii.

Stress analysis due to external loading is performed in the current study using the well-established methods for long, thin-walled, multicell box structures, such as the method outlined in Megson [8]. These stresses are superimposed on the stresses due to inflation pressure, as proposed by Comer and Levi [4] and more explicitly by Webber [5], to estimate the stress distribution throughout the aerodynamically loaded inflated wing.

Aeroelastic analysis plays an essential role in the analysis of inflatable wings. The inflated wing is typically highly flexible and may assume large elastic deformations. The elastic deformations modify the aerodynamic loading, thus affecting the stress distribution. Aeroelastic analysis in the current study is linear static analysis, based on the strip theory and typical section [9,10]. This approach is suitable for the case of high-aspect-ratio wings flying at low subsonic speeds. The shortcoming of the method is that it is suitable only for small elastic deformations, which may not be the case for inflatable wing structures. For the analysis of large deflections, the method proposed by Minguet and Dgundji [11] is adopted. Minguet and Dgundji's study investigated the static elastic behavior of composite rotor blades, which are typically slender and therefore may exhibit large deflections. The blade, or wing in the current study, is considered to be a long beam in which the deflections are a function of the spanwise coordinate. Local coordinate systems are attached to cross sections of the deflected beam, and direction cosine matrix (DCM) transformations between these local systems and a global coordinate system are used to formulate the equilibrium equations at the global system. The current study implements the strip theory and the large-deflection algorithm for aeroelastic analysis of deflections of an inflated wing and computation of the loads acting on it.

Cadogan et al. [12] and Simpson et al. [1,2] presented some analyses and test results for the mission inflatable air vehicle (MIAV) and the forward air support munition (FASM) small unmanned aerial vehicles (UAVs) incorporating multicell baffled inflated wings. The FASM has a relatively high-aspect-ratio tapered wing. The MIAV wing is straight, without initial dihedral or twist. It is of a relatively low aspect ratio, has a cambered airfoil, and is made of orthotropic polymeric material. Wing geometry and properties similar to these configurations, available from the literature, are used to set up wing configurations to be analyzed in the current study.

The novelty of the current study is in presenting an aeroelastic analysis scheme for inflated wings of the multicell baffle design, accounting for large elastic deformations. The scheme is based on classical well-established aerodynamic and structural theories and, it is hoped, can serve as an efficient design tool for inflated wings. Validation awaits wind-tunnel and flight testing.

II. Theoretical Background

Inflated-wing structures are typically membrane structures that are acted on by the internal inflation pressure and by the external aerodynamic loads. The positive inflation pressure generates tensile stresses throughout the structure, while the external loads generate both tensile and compression stresses, according to the manner in which they are applied. As a membrane, the inflated-wing structure relies on positive tensile stress to preserve its stability. Compressive stress causes local loss of stability in the form of wrinkling. A widespread wrinkled area may result in the structure collapsing. Therefore, the local stability condition is that both principal tensile stresses are positive over the whole structure. Generally speaking, the inflation pressure provides extra tensile stress to the structure, thus enabling the application of compressive loads on the structure. On the other hand, there is a limit to the tensile stress the structure can bear before mechanical failure occurs. Therefore a range of usable inflation pressures can be defined, that lies between the wrinkling and the mechanical failure limits.

Figure 1 presents the numerical scheme that is used to compute the allowable inflation pressures for a given wing configuration at various flight conditions. The numerical scheme is composed of a core algorithm (marked by a dashed frame) and a shell algorithm, operating on the core. The core algorithm computes the wing's aeroelastic loads, deflections, and stresses, for a specific wing geometry, under prescribed flow conditions and inflation pressure. The scheme starts by reading user-defined input parameters, which include wing geometry and internal cell division, structural mechanical properties, flight conditions (dynamic pressure and angle of attack), and inflation pressure. Also inputted are some numerical parameters that relate to the numerical discretization. These are discussed later on in the paper.

The core calculation starts with a static aeroelastic analysis, which yields the aeroelastic loads and deflections of the wing. Internal shear forces and moments are then calculated, based on external loads computed by the aeroelastic module. A superposition of stresses due to the external loading and due to the inflation pressure results in the stress state throughout the structure. Following a transformation to principal stresses failure criteria are applied to determine whether the wing is stable and fully elastic under the combined loads.
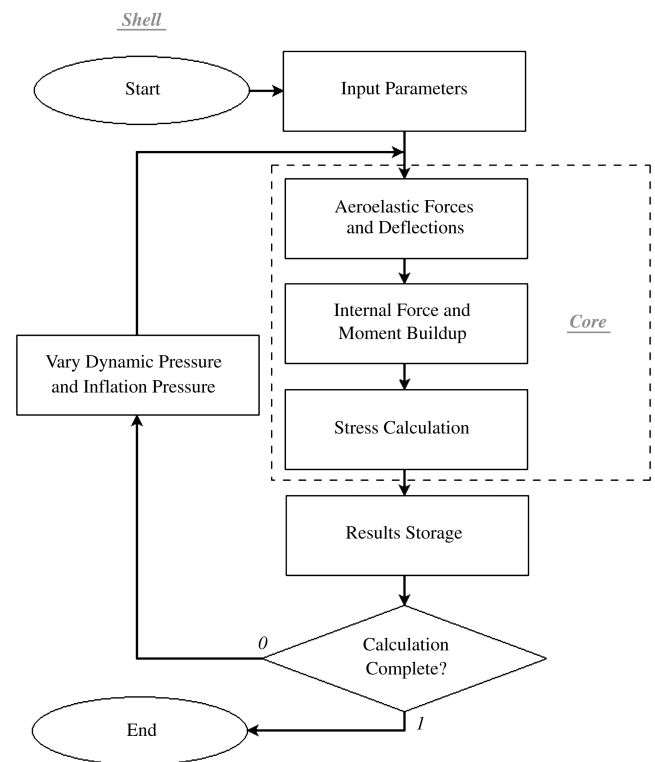

Fig. 1   Inflated-wing analysis scheme.

The shell algorithm enables repeating the core calculation for various input parameters. Typically in our analysis, the wing geometry and structural properties are held fixed, while the flow conditions and inflation pressure vary. This allows mapping of the stress states and failure criteria as functions of inflation pressure and flight dynamic pressure and plotting them as contours on a wing-loading/inflation-pressure plane (the N/S-p plane) or on a dynamic-pressure/inflation-pressure plane (the q-p plane). Of special interest are the contours of maximal principal stress and those of minimal principal stress over the structure, on the q-p plane. The contour describing the maximal principal stress that equals the material's maximal-allowed stress σ_{max} is the mechanical failure contour. The contour describing the minimal principal stress that is equal to zero is the critical wrinkling contour. These contours define regions of allowed combinations of wing loading (or dynamic pressure) and inflation pressure and also define the maximal possible wing loading for a given wing configuration.

Changing the internal pressure may raise the question of the influence of pressure on the wing geometry. When analyzing a fabricated wing this may influence the accuracy of the analysis. However, when this model is used to determine the required working inflation pressure of the wing in the design stage, any required wing dimensions can be used in the analysis. Relying on the results, the wing's fabricated dimensions can be deduced.

A. Geometric and Aerodynamic Model

The wing model used in the current study is presented in Fig. 2. The wing is assumed to be of high aspect ratio, with no taper, sweep, initial twist, or dihedral. The wing section is symmetrical, as shown in Fig. 2b, thin-walled, with a single-cell or multicell box. The
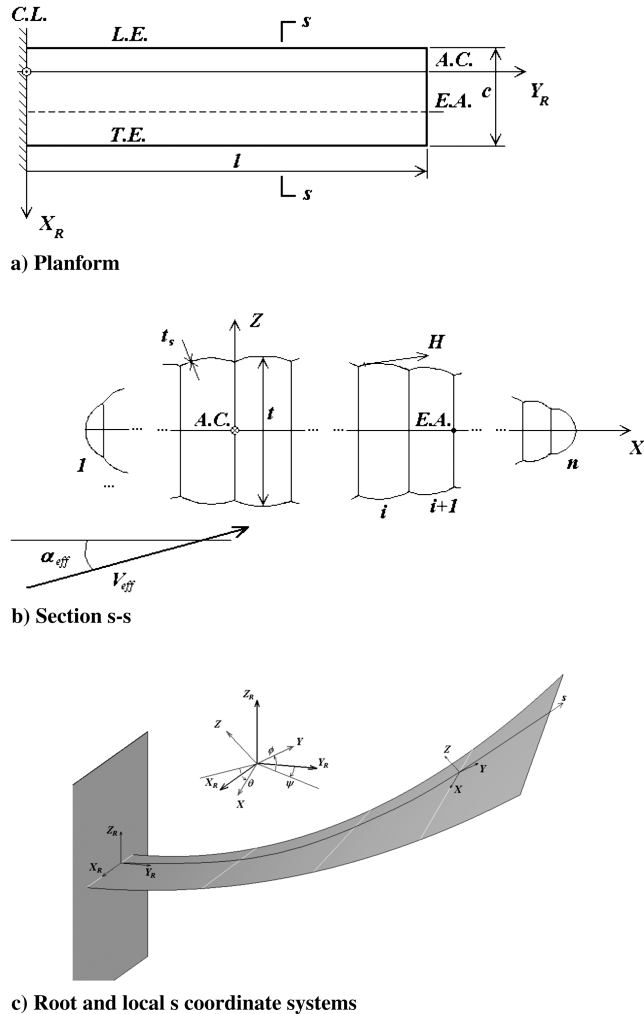

a) Planform

b) Section s-s

c) Root and local s coordinate systems

Fig. 2   Wing coordinate-system views.

multicell box design is similar to the baffle design of the ILC Dover wing presented, for example, in [12].

A root coordinate system (RCS) is defined for the wing, as shown in Figs. 2a and 2c, with its origin at the aerodynamic center of the root section. Figure 2c shows a spanwise coordinate, s, that is defined along the deformed quarter-chord line, as well as a local s coordinate system (SCS) for a general section of the wing, with its origin at the section's quarter-chord. An additional local coordinate, H, is defined tangent to the local surface in the hoopwise direction, as presented in Fig. 2b. The wing box cells are numbered 1 to n. The flow velocity is V_{eff} and the local angle of attack is α_{eff}. The analysis in this study targets flight at the low subsonic regime, neglecting compressibility effects. For simplicity, a symmetrical airfoil is used. Therefore there is no aerodynamic moment about the quarter-chord. In the implementation of large wing deflections, the following formulation was used for the calculation of angle of attack: the wing root angle of attack α is the reference angle of attack. The effective local angle of attack on a wing section at s is defined through the SCS flow velocity components as

$$\alpha_{eff} = \tan^{-1}\left(\frac{V_Z}{V_X}\right) \tag{1}$$

The velocity vector in SCS is calculated based on the root velocity vector, by using the following DCM transformation:

$$\mathbf{V}_{SCS} = DCM_{R\to s} \cdot \mathbf{V}_{RCS} \tag{2}$$

where the DCM transformation is provided by:

$$DCM\,(\psi = 0) = \begin{bmatrix} \cos\theta & 0 & -\sin\theta \\ \sin\phi\sin\theta & \cos\phi & \sin\phi\cos\theta \\ \cos\phi\sin\theta & -\sin\phi & \cos\phi\cos\theta \end{bmatrix} \tag{3}$$

The SCS effective velocity for aerodynamic computations is

$$V_{eff} = \sqrt{V_X^2 + V_Z^2} \tag{4}$$

Hence, the sectional lift force in SCS, acting at the quarter-chord is

$$L = q_{eff}cC_{l\alpha}\alpha_{eff} \tag{5}$$

where c is the chord length, and q_{eff}, the dynamic pressure, is calculated using V_{eff}. Tip effects are neglected, assuming a high-aspect-ratio wing, and the lift coefficient slope $C_{l\alpha}$ is taken as 2π for the section, corrected for finite wing. $C_{l\alpha}$ is fixed throughout the wingspan. The sectional induced drag force in SCS acting at the quarter-chord is

$$D = q_{eff}c\frac{(C_{l\alpha}\alpha_{eff})^2}{\pi AR} \tag{6}$$

Drag is not neglected in this model because it may have a significant influence on wing root moments, particularly when a wing with large deflections is considered. The lift and drag forces are transformed to chordwise (C) and normal (N) forces through the DCM transformation:

$$\mathbf{R}\,(s) = \left\{\begin{array}{c} C(s) \\ 0 \\ N(s) \end{array}\right\} = DCM_{LD\to SCS} \cdot \left\{\begin{array}{c} D(s) \\ 0 \\ L(s) \end{array}\right\} \tag{7}$$

where $DCM_{LD\to SCS}$ is the transformation matrix from wind axes to SCS. The total aerodynamic force $\mathbf{F}(s)$ at section s, created by a segment $[s, s_0]$ of the wing, is calculated by integrating the section resultants, transformed to SCS, from s to s_0:

$$\mathbf{F}\,(s) = \int_s^{s_0} DCM_{s_1\to s} \cdot \mathbf{R}\,(s_1)\,\mathrm{d}s_1 \tag{8}$$

where $s_0 > s$. The moment vector is calculated in a similar manner, with the cross product of external forces and arms, transformed to SCS:

$$\mathbf{M}(s) = \int_s^{s_0} [\text{DCM}_{s_1 \to s} \cdot \mathbf{R}(s_1)] \times [\text{DCM}_{R \to s} \cdot (\mathbf{r}(s_1) - \mathbf{r}(s))] \, ds_1 \tag{9}$$

Results of Eqs. (8) and (9) are in SCS. When assuming small deflections, Eqs. (8) and (9) may be simplified. Coordinate s becomes Y, the DCM coordinate transformations can be dropped, and the cross operation becomes a simple multiplication. When assuming small angles of attack, the forces are $N = L$ and $C = D$.

B. Structural Aeroelastic Model

The wing structure is considered in this work as a long beam. Therefore, the shear deflection can be neglected. The cross-sectional skin and webs compose a wing box, with a set of closed cells, typically termed a multicell box structure. The inflated beam-section has a tendency to assume a shape of a circular arc between webs in response to the internal pressure. A single-cell section would create a circular cylinder. The use of webs enables more control over the shape of the cylinder. Proper division of the webs and their sizes would create a shape similar to the desired airfoil, as shown in Fig. 3.

The aeroelastic analysis is based on the widely used strip theory with adaptations for large wing elastic deformations. In the strip theory model, the wing is sliced into strips in the spanwise direction. Each strip is considered a rigid two-dimensional wing section, hinged to the previous strip at the elastic axis. The hinges allow for strip motion in torsion and bending, perpendicular to the local surface, but not in the local chordwise direction. Each strip is supported by two torsion springs, modeling its elasticity in bending and in torsion. In beam theory, the following differential relations express the elastic equilibrium between moments and deflections:

$$\begin{Bmatrix} M_X(s) \\ M_Y(s) \\ M_Z(s) \end{Bmatrix} = \begin{bmatrix} EI_{XX} & & \\ & GJ & \\ & & EI_{ZZ} \end{bmatrix} \cdot \frac{d}{ds} \begin{Bmatrix} \phi \\ \theta \\ \psi \end{Bmatrix} \tag{10}$$

where ϕ, θ, and ψ are the bending angle around the SCS X axis, torsion angle around the SCS Y axis, and bending angle around the SCS Z axis, respectively. Since bending around the SCS Z axis is neglected, $d\psi/ds = 0$. Although deflections of the whole wing may be large, we assume that as long as the local curvature radius is much larger than the section's thickness, the structural decoupling between torsion and bending can be maintained.

C. Aeroelastic Equilibrium

Static aeroelastic equilibrium denotes equilibrium between the internal forces and the external loads, at every point in the structure. In the case of a wing, Eqs. (8) and (9) provide the external loads and Eq. (10) provides the internal moment buildup in the wing. Writing Eq. (9) in matrix terms and substituting into Eq. (10) yields the moment equation of equilibrium for a wing with large deflections:

$$\begin{bmatrix} EI_{XX} & & \\ & GJ & \\ & & EI_{ZZ} \end{bmatrix} \cdot \frac{d}{ds} \begin{Bmatrix} \phi \\ \theta \\ \psi \end{Bmatrix} = \int_s^l \left[[\text{DCM}_{s_1 \to s}] \cdot \begin{Bmatrix} C(s_1) \\ 0 \\ N(s_1) \end{Bmatrix} \right.$$
$$\times \left[[\text{DCM}_{R \to s}] \cdot \left(\begin{Bmatrix} X(s_1) \\ Y(s_1) \\ Z(s_1) \end{Bmatrix} - \begin{Bmatrix} X(s) \\ Y(s) \\ Z(s) \end{Bmatrix} \right) \right] ds_1 \tag{11}$$

Equation (11) is solved for the displacements at the strips' degrees of freedom for each dynamic pressure value. The aeroelastic system
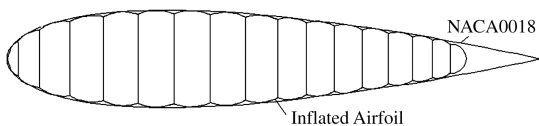
reaches equilibrium at some elastically deflected shape of the structure. There are flow conditions at which equilibrium is not reachable and the aeroelastic system diverges. Divergence typically refers to the tendency of the torsion angle to grow infinitely. It is triggered at a typical dynamic pressure value for a given wing configuration and structure. The divergence state is determined independent of the inflation pressure. This is due to the assumption that the section shape and moment of inertia do not change with inflation pressure.

When the aeroelastic system is linear, the aeroelastic equilibrium equation is typically solved in a closed form, by inversion of the aeroelastic matrix [10]. The current study aims at solving the aeroelastic equilibrium equation also for the nonlinear case of large deflections, therefore it does not rely on the closed-form solution. In the current study the aeroelastic equilibrium equation is solved iteratively, until convergence/divergence of the displacements is achieved. The solution of Eq. (11) is computed sequentially for each strip, from the wing root to the tip. An incremental strip displacement is applied to the whole wing segment spanning from the current strip to the wing tip, such that the wing segment from the strip outward is rotated as a rigid body. Convergence is declared when all incremental strip displacements become smaller than some predefined value.

Note that the current formulation is too simplistic for post-wrinkling analysis. To provide for postwrinkling analysis the formulation should account for the loss of stiffness at the wrinkled area.

The literature [8,10] provides a formula for q_d, the divergence dynamic pressure of a straight wing with small elastic deformations:

$$q_d = \frac{\pi^2 GJ}{4 \cdot \Delta x \cdot c^2 l^2 C_{L\alpha}} \tag{12}$$

where Δx is the chord-normalized distance between the aerodynamic center and the elastic axis.

When the aeroelastic analysis accounts for large wing deflections the deflections do not grow indefinitely, and divergence per se does not occur. As the wing deflects to large bending angles without mechanical failure, the effective angle of attack is reduced [13], leading to reduced torsion moment relative to the torsion moment computed by the small-deflection model. This allows the wing to find a new equilibrium, with a larger bending deflection and a lower torsion angle, instead of diverging. Divergence analysis results are presented in Sec. III of this paper.

D. Stress Computations

Following the calculation of the aeroelastic forces, section loads (internal section shear forces and moments) are calculated. The section loads allow the computation of the load-induced stresses in the structure. Since the wing structure is thin-walled, variations of stress across the membrane thickness can be neglected. This implies that the stress case is that of plane stress, for which the remaining stresses are σ_x, σ_y, and τ_{xy}, where x and y are general orthogonal coordinates to be replaced with the proper coordinates for skin or web. Stresses at each point on the wing structure are the sum of stress contributions due to load (marked by the L superscript) and due to inflation pressure [4,5] (marked by the p superscript). Thus, for the skin, the stress components are

$$\sigma_H = \sigma_H^p \qquad \sigma_Y = \sigma_Y^p + \sigma_Y^L \qquad \tau_{HY} = \tau_{HY}^L \tag{13}$$

where the subscripts H and Y indicate stresses in the hoopwise and spanwise directions, respectively. Similar expressions can be written for the webs, replacing the H subscript by Z subscript to indicate stress components in the Z direction. According to [7], the hoop stress on the skin is

$$\sigma_H^p = p \cdot \frac{r}{t_s} \tag{14}$$

where r is the local cell radius and t_s is the skin thickness. The axial stress in a cylindrical pressure vessel evolves from the force induced

Fig. 3 NACA0018 vs similar inflated section.

on the end plates by the inflation-pressure, that is distributed over the sectional walls:

$$\sigma_Y^p = p \cdot \frac{A}{A_{\text{walls}}} \qquad (15)$$

where A is the cross-sectional area, and A_{walls} is the sectional walls area.

In a single-cell section beam, the resulting axial stress is [7]

$$\sigma_Y^p = p \cdot \frac{r}{2t_s} \qquad (16)$$

In a multicell section beam, local cell radii are expected to influence the axial-stress distribution over the sectional walls. This may lead to an elaborate stress distribution function over the sectional walls and between sections. However, since the most relevant sections in terms of mechanical failure and wrinkling are expected to be close to the root section, it is possible to make use of the Saint Venant's principle, stating that at a distance larger than the largest dimension of the section acted by the loads, the stress is expected to be practically uniform throughout the section. This means that for a wing of aspect ratio higher than two, inflation pressure is expected to induce a uniform tension stress at the root section. This results in the relation presented in Eq. (15), using the relevant cross-sectional area and sectional walls area.

The Z stress over the webs due to inflation pressure (σ_Z^p) is formulated in this work. Figure 4 shows a web section between two circular cells, above the axis of symmetry. At the junction point, the ith cell creates a tensile force F_i per unit span, tangent to the skin direction $\varphi_{n,i}$. Using Eq. (14) for the definition of hoop stress, F_i is expressed as

$$F_i = pr_i \qquad (17)$$

Equilibrium of forces in Z yields

$$\Sigma F_Z = -F_i \cos \varphi_{2,i} + F_{i+1} \cos \varphi_{1,i+1} - F_{\text{web}} = 0 \qquad (18)$$

Substituting Eq. (17) into Eq. (18) yields

$$F_{\text{web}} = p(r_{i+1} \cos \varphi_{1,i+1} - r_i \cos \varphi_{2,i}) \qquad (19)$$

We note in Fig. 4 that

$$\cos \varphi_{1,i+1} = \frac{X_{i+1} - X_{\text{web},i}}{r_{i+1}} \qquad \cos \varphi_{2,i} = \frac{X_i - X_{\text{web},i}}{r_i} \qquad (20)$$

Substituting Eq. (20) into Eq. (19) and dividing by the membrane thickness t_s yields

$$\sigma_z^p = p \cdot \frac{(X_{i+1} - X_i)}{t_s} \qquad (21)$$

Equation (21) implies that the Z stress on the web is equal to the inflation pressure acting perpendicular to the line between the two
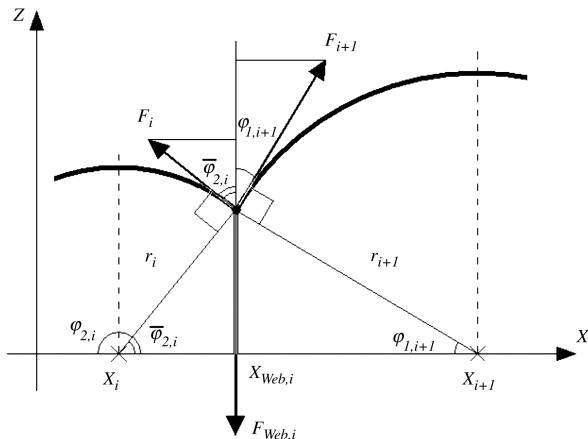

Fig. 4　Force equilibrium at a skin-web junction.

circle centers, normalized by the membrane thickness. The axial stress σ_Y^L for a symmetrical cross section is provided by [8]

$$\sigma_Y^L = \frac{M_Z X}{I_{ZZ}} - \frac{M_X Z}{I_{XX}} + \frac{P}{A_{\text{walls}}} \qquad (22)$$

The axial compression force P can be neglected when using a small-deflection scheme.

For a thin-walled structure, it is important to include the shear stress τ_{HY} in the stress calculations [8]. In the current study the shear flow integration method is used [8], which is suitable for calculating the shear stress created by shear forces acting away from the elastic axis. This method is technically elaborate, as it involves shear flow integration around the cell circumferences and the solution of a matrix system of degree $n + 1$, where n is the number of cells in the structure. This method is well established; therefore, the formulation is not recited here.

E.　Failure Criteria of an Inflated Wing

Different criteria of failure may be applied to a wing's structure: structural integrity, i.e., break or rupture, plastic deformation of wing structure, and global or local buckling are some. A characteristic of an inflated wing is high susceptibility to local buckling or wrinkling failure. At every point of the structure, the principal stress state is composed of two perpendicular components: high principal stress σ_{hi} and low principal stress σ_{lo}. Wrinkling presents a condition on the low principal stress [3]:

$$\min\{\sigma_{\text{lo}}\} \geq \sigma_w \qquad (23)$$

where σ_w is the wrinkling stress. In this work, the structural material is considered to be a membrane; hence, $\sigma_w = 0$.

There are several theories of mechanical failure regarding different types of materials in different conditions, some of which are recited in [7]. Since the material in this work is generic, a simple failure criterion is used. It should be replaced by the proper failure criterion for a specific case. The mechanical failure condition in this work presents a condition on the high principal stress:

$$\max\{\sigma_{\text{hi}}\} \leq \sigma_{\max} \qquad (24)$$

Simultaneous fulfillment of Eqs. (23) and (24) for different loading conditions creates an envelope, defining regions of allowable/required inflation pressures versus wing loading or dynamic pressures. These envelopes are used to define the maximal wing loading and the maximal inflation pressure allowed for a given wing geometry.

III.　Parametric Investigation

The algorithm for evaluation of an inflated membrane-wing's stability boundaries was coded in the Matlab software. The following subsections present a comparison with results from [5], which serves for validation, followed by demonstrative cases of single-cell and multicell elastic wings subject to aerodynamic loads. The sensitivity of the solution to physical parameters is discussed.

A.　Single-Cell-Beam Case

In this case, the wing is subject to a constant tip load and/or to a tip torsion moment. This case reduces to a tip-loaded beam with no aerodynamic loads and serves as validation of the proposed elastic model and computational scheme. The cross-sectional shape is circular. Dimensions and material properties were selected to enable comparison with the cases presented by Webber [5].

Webber [5] presented charts of results from analytical analyses and static loading experiments that were performed on inflated cylindrical cantilevered beams. The properties of the beam used are summarized in Table 1. Tables 2–4 present the critical values from Webber's charts alongside the results calculated in this work for the same loading and beam properties. The wrinkling load F_w and torsion moment T_w are seen to fit with a difference of less than 1.5%. The deflection w at incipient wrinkling can be seen to fit up to a

Table 1 Parameters of case A

Parameter	Value
Length/radius l/r	10
Radius/thickness r/t	3000
Wing span l	1.5 m
Young's modulus E	4.0 GPa
Poisson's ratio ν	0.24
Shear modulus G	1.6 GPa

Table 2 Comparison of wrinkling conditions for a circular cantilevered beam under bending

Pressure, Pa	$F_w{}^a$, N	$F_w{}^b$, N	Δ, %	$\delta_w{}^a$, mm	$\delta_w{}^b$, mm	Δ, %
6,780	24.3	24.0	1.3	13.2	13.5	−2.2
10,200	36.5	36.0	1.4	20.0	20.2	−1.0
13,500	48.4	48.0	0.8	26.0	27.0	−3.7
16,900	60.6	60.0	1.0	33.0	34.0	−2.9

[a]Results calculated in this work.
[b]Critical values from Webber's [5] charts.

Table 3 Comparison of wrinkling conditions for a circular cantilevered beam under torsion

Pressure, Pa	$T_w{}^a$, N	$T_w{}^b$, N	Δ, %	$\delta_w{}^a$, deg	$\delta_w{}^b$, deg	Δ, %
6,780	101.5	101.0	0.5	5.10	5.15	−1.0
13,500	202.0	202.0	0.0	10.18	10.30	−1.2

[a]Results calculated in this work.
[b]Critical values from Webber's [5] charts.

Table 4 Comparison of wrinkling conditions for a circular cantilevered beam under bending and torsion[a]

Pressure, Pa	$F_w{}^b$, N	$F_w{}^c$, N	Δ, %	$\delta_w{}^b$, mm	$\delta_w{}^c$, mm	Δ, %
13,500	46.0	45.0	2.2	25.0	26.0	−3.8

[a]Tip torsion moment at wrinkling: $T_w = 44$ N m.
[b]Results calculated in this work.
[c]Critical values from Webber's [5] charts.

difference of 3.8% in the combined load/torsion-moment case. The current model's deflections are all lower than Webber's results, whereas all wrinkling loads are higher. This can be attributed to the model discretization. However, differences are within the measurement inaccuracy range, as the results from the reference were taken graphically.

Webber [5] also presented a criticality condition for the wrinkling of an inflated cylindrical cantilevered beam subject to torsion moment and bending moment:

$$T^2 + 4\pi pr^3 M - 2\pi^2 p^2 r^6 = 0 \qquad (25)$$

Rearranging Eq. (25) and recalling that a lateral tip load F acting on a beam with length l yields $M_{\max} = Fl$, it is possible to express a relation between the lateral load at incipient wrinkling and the torsion moment at incipient wrinkling as

$$F_w = \frac{1}{2l}\left(\pi pr^3 - \frac{T_w^2}{2\pi pr^3}\right) \qquad (26)$$

Figure 5 shows the critical wrinkling condition line as derived from Eq. (26) and the incipient wrinkling calculated by the algorithm presented in this work. The inflation pressure used is 13.5 KPa, and the beam properties are as defined in Table 1. Load/torsion-moment combinations that lie above the presented wrinkling line result in membrane wrinkling. It can be seen that there is a correlation between the results from the proposed model and the mathematical wrinkling condition of Eq. (26). The results produced by the model

Table 5 Nominal-wing-case specification and variation

| Parameter	Value[a]
Chord c	0.33 m
Semispan l	⟨0.495⟩, 0.825, 1.155, 1.65 m
Thickness ratio t/c	12, 15, ⟨18⟩, %
Membrane thickness t_s	100, ⟨200⟩, 400, μm
Poisson's ratio ν	0.24
Wrinkle stress σ_w	0 MPa
Max stress $\sigma_{\max}$	100 MPa

[a]Angled brackets indicate nominal values.

are slightly more conservative than those of the mathematical condition, reaching a maximal difference of 1.5% in the case of pure bending, i.e., when the torsion moment is zero. This difference originates in the model discretization. Performing this calculation with a larger number of strips and sectional elements yields better accuracy.

B. Validation on a Single-Cell Box Section

A wing with dimensions typical of a small UAV [1,2,12] was selected to demonstrate the solutions produced by the presented model and computational scheme. The wing properties are presented in Table 5. The geometrical properties were varied in order to evaluate the trends of modeled wings. The nominal values of the parameters are marked in Table 5 by angled brackets.

The wing aspect ratio resulting from the specified data is between 3 and 10. The low end of this aspect ratio range is generally not considered high, as called for by the aeroelastic model assumptions. The aspect ratio values were selected considering the existing applications mentioned before, such as the MIAV, whose aspect ratio is between three and four, depending on configuration. Moreover, computations of wings with aspect ratios higher than seven resulted in either unreasonably small allowed dynamic-pressure range or in very high required inflation pressure, requiring membrane thickness that exceeds the thin-wall assumption limits. The fact that inflated wings tend to be of low-aspect-ratio calls for replacement of the strip theory with a higher-fidelity method that is able to reliably handle low-aspect-ratio wings.

The structural single-cell section radius is 0.14 of the reference chord. Nominal membrane thickness is 200 μm, and the material Young's modulus is 0.2 GPa. A very low Young's modulus was chosen in order to evoke large wing deflections, thus demonstrating the differences between small- and large-deflection models. The number of strips along the semispan is 50, the number of circumferential elements is 50, and the maximal-allowed iterations in the aeroelastic algorithm is 200. Figure 6 shows the wing section and
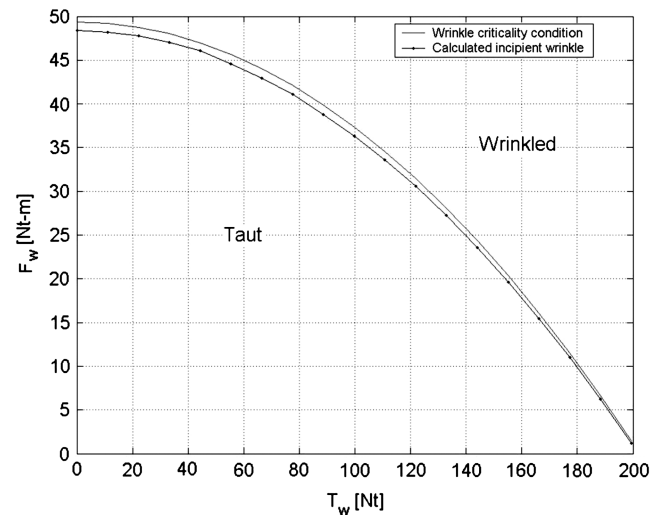
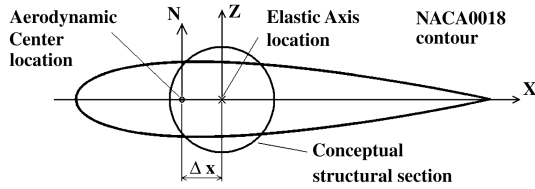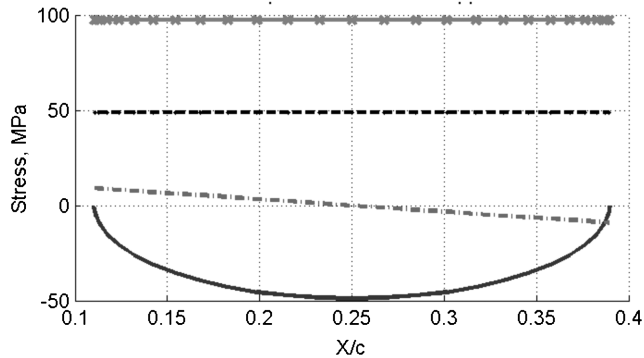**Fig. 5 Combined bending-torsion criticality condition for an inflated circular cantilever beam.**

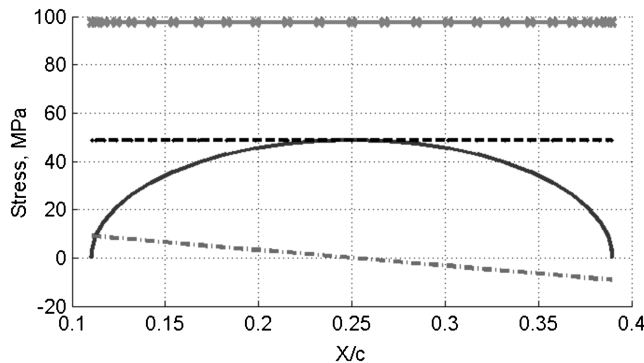Fig. 6 Single-cell wing section model.

the conceptual single-cell inflated section. Aerodynamic normal force N is acting at the wing's aerodynamic center. Δx is the chord-normalized distance between the aerodynamic center and the elastic axis of the structural section. When the elastic axis is behind the aerodynamic center Δx is positive, and torsion moment about the elastic axis acts on the beam.

1. Section Subject to Zero Torsion Moment

Validation of the numerical scheme is performed on a single-cell structure. The presented calculation is performed with an assumption of small deflections, neglecting drag and chordwise forces. The aerodynamic force calculation is based on the presented wing chord, while all the structural calculations are done on the circular beam. In this case the structural section is located such that $\Delta x = 0$, so that no torsion moment acts on the section. Figure 7 presents the stress components according to their origin and direction, over the wing root section. Hoop-stress value is 97.53 MPa, which is about 97.5% of the maximal-allowed stress (see in Table 5). The axial stress due to inflation pressure is half the hoop stress, as expected from comparing Eqs. (14) and (16). The axial stress due to the bending moment varies proportionally to $Z(X)$. This is seen in Fig. 7 as an ellipse. This result

a) Upper skin

b) Lower skin

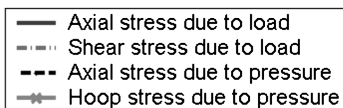|	
——	Axial stress due to load
—·—·	Shear stress due to load
- - - -	Axial stress due to pressure
—✳—✳	Hoop stress due to pressure

Fig. 7 Stress components over the wing root section, with no torque, at maximal-allowed dynamic pressure.

is in agreement with Eq. (22), under the assumption of small deflections.

A positive shear stress is defined in the circumferential counterclockwise direction. Therefore, shear stress at symmetric points respective to the Z axis have an identical value and an opposite sign. Shear stress created by the applied shear force is zero on the section's intersection points with the Z axis. The maximum value of the shear stress is approximately 9 MPa, at the upper and lower skin junctions. Between these extremes the shear stress changes linearly and symmetrically around the section.

Figure 8 shows the principal stresses over the wing-root section and the angle of high principal stress. The shapes seen in the principal stress plot can vary considerably. However, identification of several points on the plot can provide important information about the state of the wing. The symmetry of the load in this case leads to symmetrical stress. Since the load on the wing acts upward, the minimum stress point is seen on the upper skin, at $X/c = 0.25$.

A low principal stress with a minimum value of zero, as seen in Fig. 8a, is the indication of incipient wrinkling of the inflated membrane structure. The stress angle, seen in Fig. 8b, at the area that experiences incipient wrinkling is expected to be equal to the angle of visible wrinkles [3,5,6]. In this case the angle is zero at the upper skin, $X/c = 0.25$, i.e., the wrinkles are expected to appear in the local X direction, or hoop direction. This result is in agreement with [3–6].

The maximal principal stress is found on the lower skin, at $X/c = 0.154$, as seen in Fig. 8a. This location is equivalent to a circumferential angle φ of approximately $45°$. The value of the maximal principal stress is 100 MPa, identical to the defined maximal-allowed stress for the wing. Therefore, mechanical failure is expected to appear at $\varphi \approx 45°$ and/or at symmetrical location with respect to the Z axis. The high-principal-stress value is very close to the hoop-stress value, implying that the hoop stress is the prime contributor to mechanical failure. The situation of simultaneous fulfillment of both failure conditions indicates that the wing is at its maximal-allowed loading, as will be shown later in the paper.

2. Section Subject to Positive Torsion Moment, Small-Deflection Model

Stress analysis is performed for a single-cell inflated wing at a $16°$ angle of attack. In this case $\Delta x = 0.09$; hence, the aerodynamic torsion moment is positive, creating wing-tip wash-in. Calculations are under the assumption of small deflections. Figure 9 presents stress contours on the q-p plane, showing high and low principal stresses. The maximum high and minimum low principal stresses are marked. The maximal-allowed inflation pressure p_{max} is found at zero dynamic pressure; hence, it is determined by the hoop stress alone. The maximal-allowed dynamic pressure q_{max} in this case is 143 Pa, corresponding to inflation pressure of 421 KPa.

The aeroelastic scheme of this study determines the divergence dynamic pressure by computing and monitoring the torsion-angle distribution along the wingspan, at each aeroelastic iteration. It was arbitrarily decided that whenever the torsion angle at any span location exceeds $90°$, wing divergence is identified. Dynamic pressure at the identified divergence state is shown in Fig. 9 as a vertical line, marked $q_d(\alpha = 16°)$. For the current case divergence was reached at a dynamic pressure of $q \approx 320$ Pa. This value of dynamic pressure is about 20% below the theoretical divergence value calculated from Eq. (12) based on the wing's torsional stiffness of $GJ = 10$ N-m^2. It was found that as the root angle of attack is reduced to zero, the divergence dynamic pressure approaches the theoretical value as calculated by Eq. (12).

The stress contours are bounded at $q = q_d(\alpha)$, making the divergence line an asymptote to the principal stress contours. The logic behind this observation is as follows: divergence represents an exponential growth of the aerodynamic forces and wing deflections. This leads to an exponential growth of the stress values. In Eq. (22), for instance, an infinite moment M_z leads to infinite values of the stress σ_Y^L at positive and negative Z locations. This means that at the identified divergence dynamic-pressure value, the inflation pressure required to resist the stress imposed by the infinite loading also has to be infinite.

a) **Principal stresses, high (left) and low (right) and symmetry line**
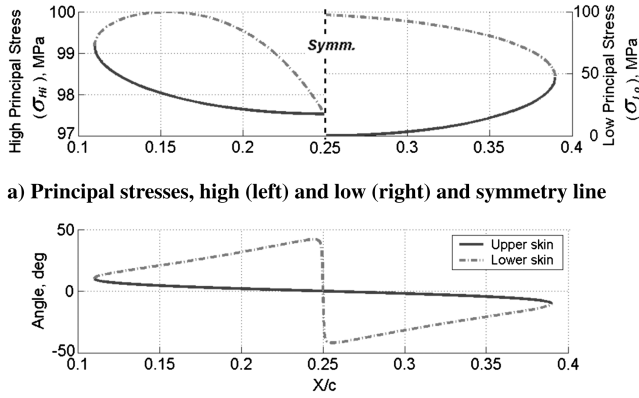
b) **Principal coordinate system angle**

Fig. 8   Principal stresses and stress angle over the wing root section, for a wing with a single-cell section and no torsion moment (symmetric case) at maximal-allowed dynamic pressure.
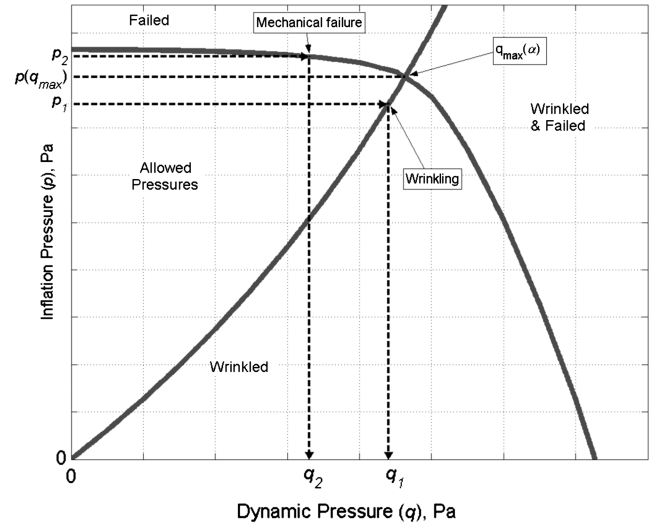
It can be seen that the critical wrinkling contour ($\sigma_{lo} = 0$) and the mechanical failure contour ($\sigma_{hi} = \sigma_{max}$) have a typical shape, creating, along with the p axis, a half-diamond-shaped envelope of allowed stresses (see also Fig. 10). This typical contour combination will henceforth be termed the stress envelope on the q-p plane. Later in the paper, envelopes are presented on the wing-loading/inflation-pressure (N/S-p) plane as well.

Observing the stress envelopes on the q-p plane provides some insight on the wing failure modes at different inflation pressures. Figure 10 presents the method for identifying the failure mode for a prescribed inflation pressure. When inflating the wing to a pressure that is below $p(q_{max})$ (see p_1 in Fig. 10), exceeding the allowed dynamic pressure (q_1) leads to wrinkling of the structure and danger of wing collapse, which may be fully recoverable when the conditions return to an allowed q and α combination. When the inflation pressure is above $p(q_{max})$ (see p_2 in Fig. 10), exceeding the allowed dynamic pressure (q_2 in Fig. 10) would result in an irrecoverable mechanical failure damage to the structure in the form of plastic deformation or structural integrity failure. It may seem that mechanical failure is expected when continuing to increase the dynamic pressure above q_1 as well, but this conclusion cannot be drawn here, since the analysis in this work does not include postwrinkling calculations.

Figure 11 presents the stress contours on the wing-load/inflation-pressure (N/S-p) plane. The wrinkling limit and the mechanical failure contours, as well as the p_{max} point, can be seen as in the q-p
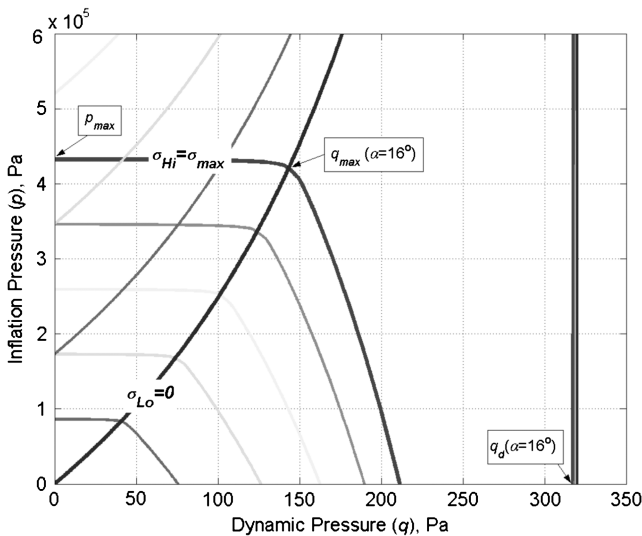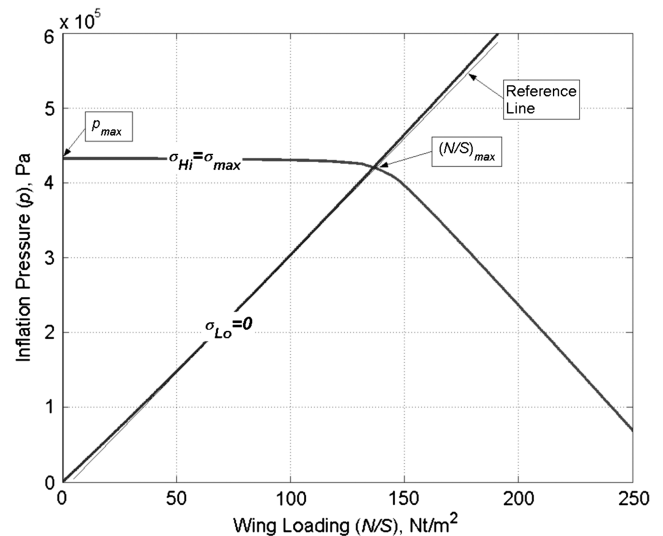

Fig. 10   Failure modes of the inflated wing.

plane (Fig. 9). In this case $(N/S)_{max} = 137$ N/m² at $p = 421$ KPa. The σ_{lo} contours are not entirely linear, as evident by the linear reference line drawn near the critical wrinkling contour. The slight curvature can be explained with the relation $N/S = C_L q$. For a rigid wing the lift coefficient per wing-root angle of attack is independent of the dynamic pressure. In this case, wing loading is a linear function of the dynamic pressure. For the elastic wing considered here, the aeroelastic torsion of the wing changes the angle of attack distribution over the wingspan, thus changing the lift coefficient as a function of the dynamic pressure, and the wing loading is no longer a linear function of dynamic pressure.

3.   Section Subject to Positive Torsion, Large-Deflection Model

Figure 12a presents the deflections calculated by the wing solution scheme, alternately using a large-deflection calculation (LDC) model or a small-deflection calculation (SDC) model for the aeroelastic calculation. Figure 12b presents the wing-tip torsion angle from the two calculations. The SDC results show an increase of the Z deflection and of the torsion angle toward divergence. Notably, at dynamic pressure of about 100 Pa, the Z deflection crosses the physical limit of 100% semispan. On the other hand, the LDC Z deflection is seen to gradually converge toward the physical limit, or even below it, with increased dynamic pressure. The increase of the Z deflection occurs due to the aeroelastic increase in the torsion angle

Fig. 9   Contours of the high and low principal stresses on the q-p plane, for a wing at $\alpha = 16°$ and subject to positive torsion moment, under the assumption of small deflections; $\sigma_{max} = 100$ MPa.

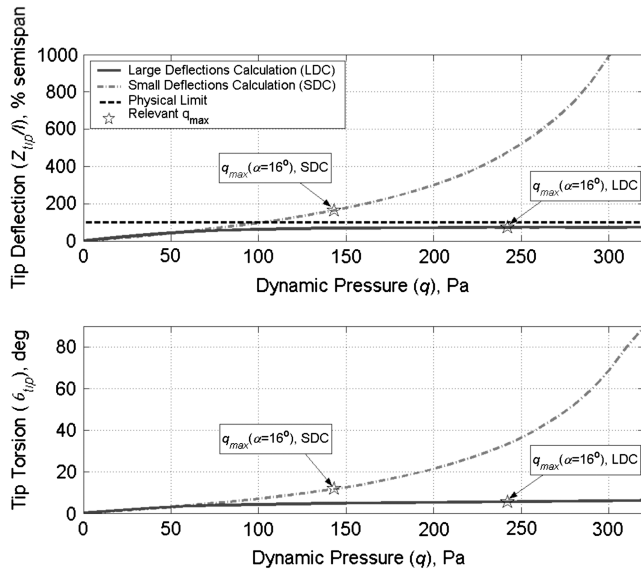**Fig. 11   Maximum high and minimum low principal stresses on the N/S-p plane, for a wing at $\alpha = 16°$ and subject to positive torsion moment, under the assumption of small deflections; $\sigma_{max} = 100$ MPa.**

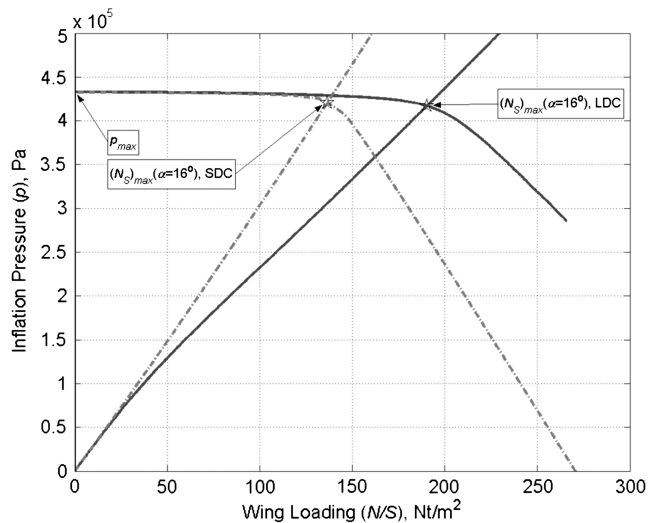**Fig. 12 Wing-tip deflection and torsion angle for small and large-deflection calculations.**

Fig. 13 Stress envelopes on the N/S-p plane for small and large-deflection calculations.

with dynamic pressure. The aerodynamic loads computed by the LDC are significantly lower than those computed by the SDC for high dynamic pressure values. This is due to the decrease in the local angle of attack with increasing bending angles. It can be viewed as an aeroelastic stiffening that takes place for large bending angles. This reduces the tendency of the wing to develop torsion angles, thus reducing the aeroelastic loads and wing deflection.

The value of the maximal-allowed dynamic pressure for the LDC is 242 Pa, which is approximately 70% higher than that of the SDC. The tip deflection at this point is 72% semispan for the LDC, while for the SDC the tip deflection exceeds the physical limit of 100%

semispan. The tip torsion angle is 5.5° for the LDC, which is about 53% less than that of the SDC. The SDC is significantly more conservative than the LDC, predicting larger deflections and a lower maximal-allowed dynamic pressure when the wing's elastic deformations are considerable.

Figure 13 presents the critical stress contours created by alternately using the LDC and SDC schemes, on the N/S-p plane. The two calculations produce similar results on low dynamic-pressure values. This similarity is indicative of the match between the schemes when deflections are small. However, with the rise of dynamic pressure, the N/S_{max} point of the SDC is at lower dynamic pressure than that of the LDC. This difference is attributed to the excessive increase of torsion angle in the SDC as discussed earlier. Prediction of an excessive torsion angle leads to increased-aerodynamic loads, thus causes a premature predicted failure.

C. Investigation of a Multicell Box Section

The presented scheme was used to demonstrate results for an inflated wing with a multicell box section. Wing properties are with some similarity to data appearing in [1,2,12] of the MIAV wing. Unfortunately, some important dimensions and mechanical properties of the wing material were not available in these references, so that direct comparison could not be performed. Additionally, no treatment of incipient wrinkle or mechanical failure is considered in these references.

The wing is rectangular with properties as specified in Table 5. Young's modulus is 1 GPa. The airfoil shape is from the symmetric NACA four-digit family, with varying thickness ratios. The inflated airfoil is composed of 14 cells, with webs at locations similar to web locations of [12]. The analysis was based on 50 spanwise strips. The skin sections were modeled by 10 elements per cell (five on the upper skin and five on the lower skin). The webs were modeled by a single element each, with two control points, at the top and bottom of the web. Up to 200 aeroelastic iterations were run to convergence. The relatively small number of strips and elements was chosen due to the limited computational resources available to the authors. The structural section shape is as shown in Fig. 14.

All calculations for the multicell wing were performed using the LDC model. Elastic axis is at 0.384 of the wing chord, i.e., $\Delta x = 0.134$. The torsion rigidity GJ of this section is 140 N · m^2, yielding a theoretical divergence dynamic pressure of 2.43 KPa for the nominal wing.

1. Effect of Aspect Ratio

The effect of aspect ratio on the pressure envelope was studies by comparing results of wings of four aspect ratio values: 3, 5, 7, and 10, at an angle of attack of 16°. The aspect ratio was altered through change of the wing span. The cross-sectional shape and chord length were not changed, therefore the sectional rigidity (EI, GJ) remained fixed. Figure 15a presents the wing-tip deflections, normalized by the respective semispan in percentages of the semispan. It can be seen that the higher the wing aspect ratio, the larger the normalized deflection for a given dynamic pressure. This can be understood from the first row of Eq. (10). Since a higher moment acts on an unchanged EI when the aspect ratio is increased, the curvature $d\phi/ds$ becomes larger, leading to a larger tip deflection. The tip torsion angles are small, less than 0.6° at q_{max} for all aspect ratios (Fig. 15b).

Stars mark the points at which the wing is at q_{max}. q_{max} values were found using the stress envelope on the q-p plane, as presented earlier.
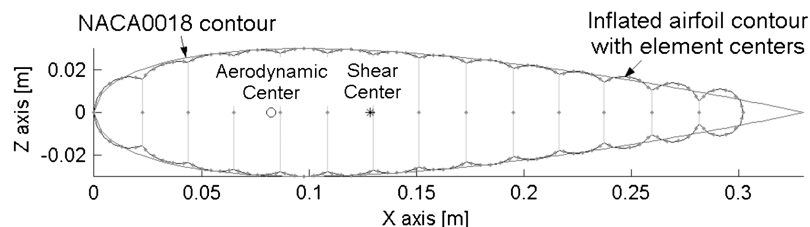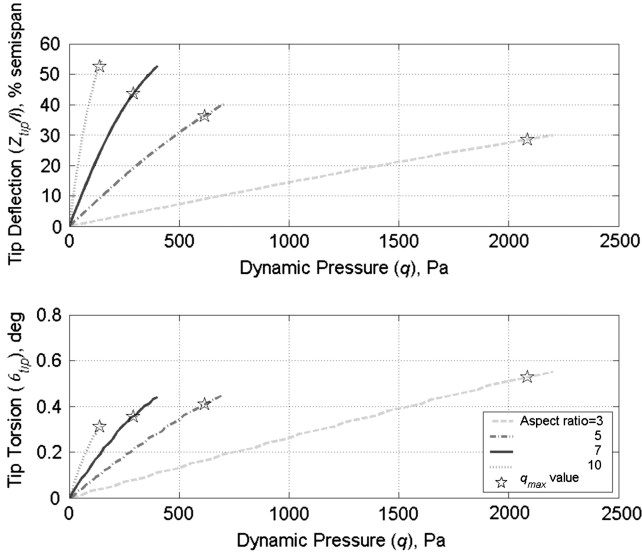

Fig. 14 Multicell box cross-sectional shape.

Fig. 15 Wing-tip deflection and torsion angle for wings with different aspect ratios.

q_{max} is seen to significantly decrease with increase of aspect ratio. Using the definition of dynamic pressure, the maximal-allowed flight velocity can be deduced:

$$V_{max} = \sqrt{\frac{2q_{max}}{\rho}} \quad (27)$$

where ρ is the air density at the flight altitude. When relating V_{max} to aspect ratio it was found that V_{max} is proportional to the inverse of the aspect ratio, up to the numerical accuracy.

Figure 16 presents the stress envelopes on the N/S-p plane. The maximal wing loading is significantly decreased with increasing aspect ratio, similarly to the decrease of q_{max}. The maximal inflation pressure of 670 KPa is identical for all aspect ratio values. This is because changing the wing span does not influence the cell radius or the membrane thickness. Hence, according to Eq. (14), it has no influence on the hoop stress, which is the dominant stress component in the near-horizontal region of the envelope.

As mentioned previously, for the wing with a single-cell section, the increase of the torsion angle when the wing approaches divergence is the reason for curvature of the σ_{lo} contours. Use of the LDC scheme introduces the effective angle of attack reduction
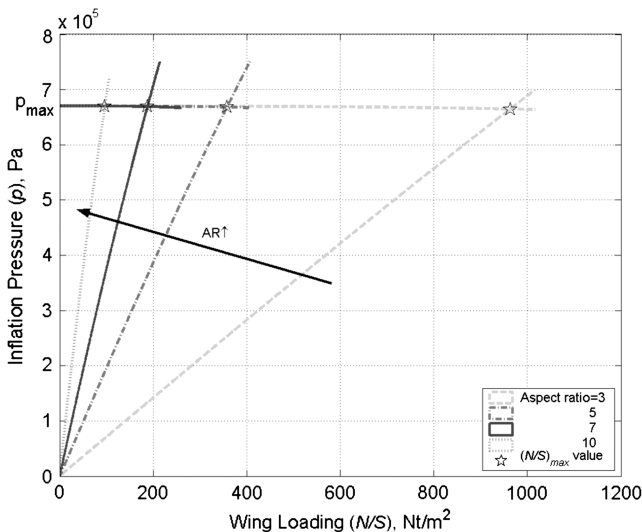
mechanism, which reduces the tendency of the wing to twist. This changes the behavior of the wing at q_d from divergence to a new state of equilibrium with very deep deflection and a small torsion angle. In the presented case, the theoretical divergence dynamic pressure of the nominal wing is far higher than the resulting maximal-allowed dynamic pressure of the wing. This, in combination with the use of the large-deflection scheme, leads to contours with curvature that is hardly noticeable in the scale of the stress envelope on the q-p or N/S-p plane.

2. Effect of Airfoil Thickness Ratio

Figure 17 shows the allowed q-p envelopes for three airfoil thickness ratios: 12, 15, and 18%. The thickness ratio is changed by changing the airfoil thickness while maintaining a constant chord length. The airfoil thickness is defined as twice the largest cell radius in the section. Figure 17 shows that the maximal-allowed inflation pressure decreases with increased thickness ratio. This drop occurs because the change of the largest cell radius, proportional to the change of the thickness ratio, leads to a proportional increase of the hoop stress for a given inflation pressure [Eq. (14)]. Since maximal-allowed inflation pressure occurs at $q = 0$, the hoop stress is the largest stress component dominating the mechanical failure at this point. To maintain the hoop stress equal to σ_{max}, when cell radius changes the inflation pressure has to change in the opposite direction.

The slope of the wrinkling-limit contours is seen to drop with the increase of thickness ratio. Substituting Eqs. (22) and (15) into the expression for the axial stress in Eq. (13) and neglecting the compressive stress due to the compressive force and due to the Z moments yields

$$\sigma_Y = -\frac{M_X Z}{I_{XX}} + p \frac{A}{A_{walls}} \quad (28)$$

The first term is the stress due to the bending moment (M_X). The second term is the tension stress due to internal pressure. For the simplicity of the explanation of this trend we shall use a single-cell section. The circumferential location of incipient wrinkling is $\varphi = \pi/2$. Using the expression for moment of inertia and transforming to polar coordinates around the center of area of the section yields

$$\sigma_Y = -\frac{M_X}{\pi r^2 t_s} + p \frac{r}{2t_s} \quad (29)$$

An increase in r leads to a decrease of the stress due to bending moment according to $1/r^2$ and to an increase in the stress due to inflation pressure according to r. Consequently, the ability of the tension stress due to inflation pressure to resist the compression stress
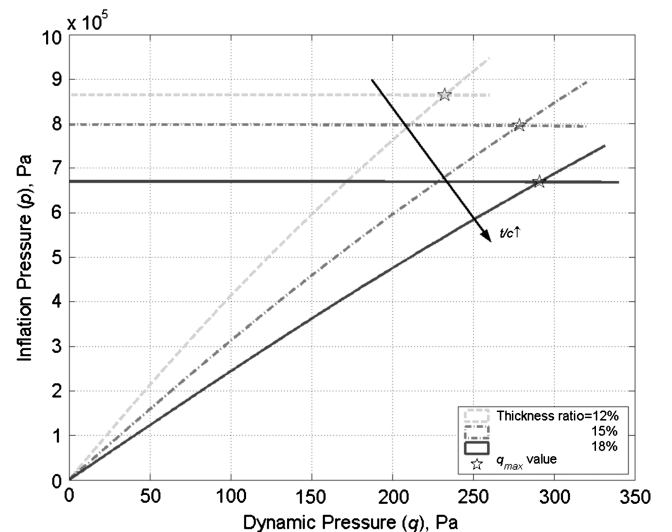
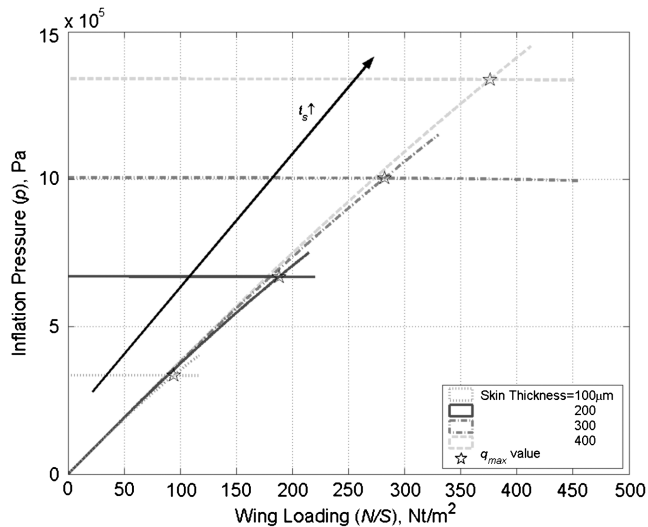

Fig. 16 Stress envelopes on the N/S-p plane for a wing with a multicell box section and of different aspect ratios.

Fig. 17 Stress envelopes on the q-p plane for a wing with a multicell box section and of different thickness ratios.

Fig. 18 Wing-loading envelopes for a wing with a multicell box section of different membrane thicknesses.

due to bending moment increases with increasing sectional thickness ratio. This leads to a higher value of dynamic pressure that can be carried by a wing inflated to a prescribed pressure, i.e., reducing the slope of the wrinkling-limit contour.

The value of q_{max} is therefore determined by two opposite trends. As thickness increases the inflation pressure for mechanical failure drops, thus the mechanical failure contour intersects with the wrinkling-limit contour at a lower dynamic pressure. Concurrently, the reduced slope of the wrinkling-limit contour increases the dynamic-pressure value at the intersection. It is seen that in the studied case, the increase of q_{max} is the dominant trend.

3. Effect of Membrane Thickness

Figure 18 presents the influence of the membrane thickness on the stress envelope presented on the N/S-p plane. The wrinkling-limit contour remains practically unchanged with membrane thickness variation. Consequently it can be deduced that membrane thickness variation cannot be used to influence the wing's wrinkling load.

The mechanical failure contour values expand linearly with membrane thickness variation. Consequently $(N/S)_{max}$ is practically proportional to the membrane thickness, along with the inflation pressure at $(N/S)_{max}$. This implies that the membrane thickness can be used to alter the mechanical failure contour's pressure values and increase the maximal wing loading.

IV. Conclusions

A methodology was presented for aerostructural analysis of inflated wings. The methodology involves computation of the aeroelastic force equilibrium on an inflated wing, accounting for large wing deflections and analysis of stresses due to aeroelastic loads and due to inflation pressure. The analysis is based on a beam theory and an aerodynamic strip theory. Wrinkling criterion and mechanical failure criterion are used to define the pressure envelope, which identifies regions of allowed combinations of wing loading and inflation pressure for a given wing geometry and material properties. The pressure envelope can be a valuable tool in the design and analysis of inflated wings as it defines the maximal wing loading a wing can carry, together with the corresponding required (and maximal-allowed) inflation pressure.

The methodology was used to investigate the characteristics of single-cell and multicell inflated wings of various aspect ratios, airfoil thickness ratios, and membrane thicknesses. It was found that increased aspect ratio (through increased span) significantly decreases the maximal-allowed wing loading. Inflated wings seem to be most effective in the domain of low aspect ratio. Increased airfoil thickness ratio was shown to provide limited improvement in the

maximal-allowed wing loading. Increased membrane thickness was shown to allow higher maximal wing loading by enabling the use of a higher inflation pressure.

It was shown that wrinkling of an inflated wing is mainly dominated by the balance of compressive stress at wing root, originating mainly from bending moment, and tensile axial stress originating from the inflation pressure. Wing mechanical failure is mainly dominated by tensile hoop stress originating from the inflation pressure. In addition, it was shown that a positive torsion moment on the wing further limits the wing's loading and poses constraints on the maximal and minimal inflation pressures. It was shown that for a given design geometry and material there is an optimum inflation pressure in terms of maximal wing loading. Exceeding it results in sensitivity to mechanical failure, while using a lower pressure results in increased sensitivity to wrinkling.

It was demonstrated that using a calculation that is based on the assumption of small deflections predicts maximal-allowed wing loading that is significantly lower than the maximal-allowed wing loading computed by accounting for large deflections. It is therefore suggested that using a small-deflection calculation leads to excessively conservative results when wing deflections are large.

Future work will involve improvement of the aeroelastic model to better handle low-aspect-ratio configurations and expansion of the structural model to handle asymmetrical airfoils and more complex geometries. Finally, modeling of the range between the incipient wrinkling and complete wing collapse is suggested in order to investigate the ability to expand the allowed wing loading and dynamic pressure ranges.

References

[1] Simpson, A. D., Smith, S. W., and Jacob, J., "Aeroelastic Behavior of Inflatable Wings: Wind Tunnel and Flight Testing," 45th Aerospace Sciences Meeting and Exhibit, Reno, NV, AIAA Paper 2007-1069, 2007.

[2] Simpson, A. D., Jacob, J., and Smith, S. W., "Flight Control of a UAV with Inflatable Wings with Wing Warping," 24th AIAA Applied Aerodynamics Conference, San Francisco, AIAA Paper 2006-2831, 2006.

[3] Stein, M., and Hedgepeth, J. M., "Analysis of Partly Wrinkled Membranes," NASA, 1961.

[4] Comer, R. L., and Levy, S., "Deflections of an Inflated Circular-Cylindrical Cantilever Beam," *AIAA Journal*, Vol. 1, No. 7, July 1963, 1652–1655.
doi:10.2514/3.1873

[5] Webber, J. P. H., "Deflections of Inflated Cylindrical Cantilever Beams Subjected to Bending and Torsion," *The Aeronautical Journal*, Vol. 86, No. 858, 1982, 306–312.

[6] Veldman, S. L., "Wrinkling Predictions of Cylindrical and Conical Inflated Cantilever Beams Under Torsion and Bending," *Thin-Walled Structures*, Vol. 44, No. 2, 2006, 211–215.
doi:10.1016/j.tws.2006.01.003

[7] Harvey, J. F., *Theory and Design of Modern Pressure Vessels*, Van Nostrand Reinhold, New York, 1974, Chap. 5.

[8] Megson, T. H. G., *Aircraft Structures and Engineering for Students*, Arnold, London, 1999, Chaps. 9, 10.

[9] Bismarck-Nasr, M. N., *Structural Dynamics in Aeronautical Engineering*, AIAA Education Series, AIAA, New York, 1999.

[10] Bisplighoff, R. L., Ashley, H., and Halfman, R. L., *Aeroelasticity*, Dover, Mineola, NY, 1996.

[11] Minguet, P., and Dgundji, J., "Analysis for Composite Blades Under Large Deflections Part I: Static Behavior," *AIAA Journal*, Vol. 28 No. 9, Sept. 1990, 1573–1579.
doi:10.2514/3.25255

[12] Cadogan, D. P., Scarborough, S. E., Gleeson, D., and Dixit, A., "Recent Development and Testing of Inflatable Wings," 47th AIAA/ASME/ASCE/AHS/ASC Structures, Structural Dynamics, and Materials Conference, Newport, RI, AIAA Paper 2006-2139, 2006.

[13] Thwapiah, G., and Campanile, L. F., "Nonlinear Aeroelastic Behavior of Compliant Airfoils," *Smart Materials and Structures*, Vol. 19, No. 3, 2010, pp. 1–9.